A&A 470, 957–963 (2007)
DOI: 10.1051/0004-6361:20066574
© ESO 2007

Astronomy & Astrophysics

Near-infrared polarimetric study of the bipolar nebula IRAS 19312+1950⋆

K. Murakawa[1], J. Nakashima[2], K. Ohnaka[1], and S. Deguchi[3]

[1] Max-Planck-Institut für Radioastronomie, Auf dem Hügel 69, 53121 Bonn, Germany
e-mail: murakawa@mpifr-bonn.mpg.de
[2] Academia Sinica Institute of Astronomy and Astrophysics, PO Box 23-141, Taipei, Taiwan
[3] Nobeyama Radio Astronomy, National Astronomical Observatory of Japan, Minamimaki, Minamisaku, Nagano 384-1305, Japan

Received 16 October 2006 / Accepted 23 April 2007

ABSTRACT

Aims. We have investigated the properties of the central star and dust in the bipolar nebula IRAS 19312+1950, which is an unusual object showing the characteristics of a supergiant, a young stellar object, and an asymptotic giant branch (AGB) star.
Methods. We obtained *H*-band polarimetric data of IRAS 19312+1950 using the near-infrared camera (CIAO) on the 8 m Subaru telescope. In order to investigate the physical properties of the central star and the nebula, we performed radiative transfer modeling and compared the model results with the observed spectral energy distributions (SEDs), the radial profiles of the total intensity image, and the fraction of linear polarization map.
Results. The total intensity image shows a nearly spherical core with ∼3″ radius, an S-shaped arm extending ∼10″ in the northwest to southeast direction, and an extended lobe towards the southwest. The polarization map shows a centro-symmetric vector alignment in almost the entire nebula and low polarizations along the S-shaped arm. These results suggest that the nebula is accompanied by a central star, and the S-shaped arm has a physically ring-like structure. From our radiative transfer modeling, we estimated the stellar temperature, the bolometric luminosity, and the current mass-loss rate to be 2800 K, 7000 $L_{\odot}$, and 5.3×10^{-6} $M_{\odot}$ yr^{-1}, respectively.
Conclusions. Taking into account previous observational results, such as the detection of SiO maser emissions and silicate absorption feature in the 10 μm spectrum, our dust radiative transfer analysis based on our near-infrared imaging polarimetry suggests that (1) the central star of IRAS 19312+1950 is likely to be an oxygen-rich, dust-enshrouded AGB star and (2) most of the circumstellar material originates from other sources (e.g. ambient dark clouds) rather than being a result of mass loss from the central star.

Key words. polarization – radiative transfer – stars: AGB and post-AGB

1. Introduction

IRAS 19312+1950 is a peculiar bipolar nebula with a horn-like appearance extending ∼30″ in the 2MASS *JHK*-band images. With IRAS colors [12] − [25] = 0.50 and [25] − [60] = 0.71, it falls into region VIII on the IRAS color–color diagram (van der Veen & Habing 1988). A relatively large fraction of objects in this region is known to belong to different types, such as Miras, OH/IR stars, or carbon stars. A weak 10 μm absorption was detected in the IRAS low-spectral resolution spectrum (LRS) of IRAS 19312+1950 (Volk et al. 1991). Maser emissions of silicon monoxide (SiO), water (H_2O) (Nakashima & Deguchi 2000), and hydroxyl (OH) (Lewis, B. M., private communication) were also detected.

These observational results led the authors to conclude that IRAS 19312+1950 is a candidate for an oxygen-rich asymptotic giant branch (AGB) or post-AGB star (Nakashima & Deguchi 2000). However, some unusual characteristics have been found in subsequent observations, and debates on the true nature of IRAS 19312+1950 have arisen. Deguchi et al. (2004) found C-, N- and O-bearing molecules (e.g. $H^{13}CN$, CH_3OH, SO, and SO_2) towards this object. C- and N-bearing molecules such as $H^{13}CN$ and CH_3OH are often detected in carbon-rich circumstellar environments or in molecular cloud cores in a dark cloud. While C-bearing molecules and SO take ∼10^5 yr and ∼10^6 yr, respectively, to be formed in an environment like a dark cloud, the time it takes (∼10^4 yr) for expanding gas with an expansion velocity of 10 km s^{-1} to cross the envelope of IRAS 19312+1950 (∼5.8×10^{17} cm at 2.5 kpc, Nakashima et al. 2004) is remarkably shorter than the above time scales. Furthermore, a stellar velocity of ∼36 km s^{-1} was found from the velocity components of the SiO and H_2O masers. Besides the broad component in the thermal emission of some molecules, the presence of a narrow component in the thermal emission of CO, HCN, CS, SO, and HCO^+ suggests the presence of an additional, kinematically cold component, which has been interpreted as originating from a dust cloud rather from than the matter ejected by mass loss from the central star (Nakashima & Deguchi 2000; Deguchi et al. 2004). In addition, Deguchi et al. (2004) estimated the envelope mass and the mass-loss rate to be ∼25 $M_{\odot}$ and ∼2.6×10^{-4} $M_{\odot}$ yr^{-1}, respectively, by means of the large-velocity-gradient (LVG) model with their observational results of several molecular lines in the radio frequency domain. For the above reasons, to date, it seems plausible that IRAS 19312+1950 is a progenitor with an initial mass of $M_{\star} \geq 4$ $M_{\odot}$ and has been embedded in an ambient cloud by chance (see also Nakashima & Deguchi 2005).

Previous studies of this object have mainly focused on identifying gas-phase molecules and investigating of their kinematics. In order to better understand this object's nature, model analyses

⋆ *H*-band polarization data is only available in electronic form at the CDS via anonymous ftp to
cdsarc.u-strasbg.fr (130.79.128.5) or via
http://cdsweb.u-strasbg.fr/cgi-bin/qcat?J/A+A/470/957

Article published by EDP Sciences and available at http://www.aanda.org or http://dx.doi.org/10.1051/0004-6361:20066574

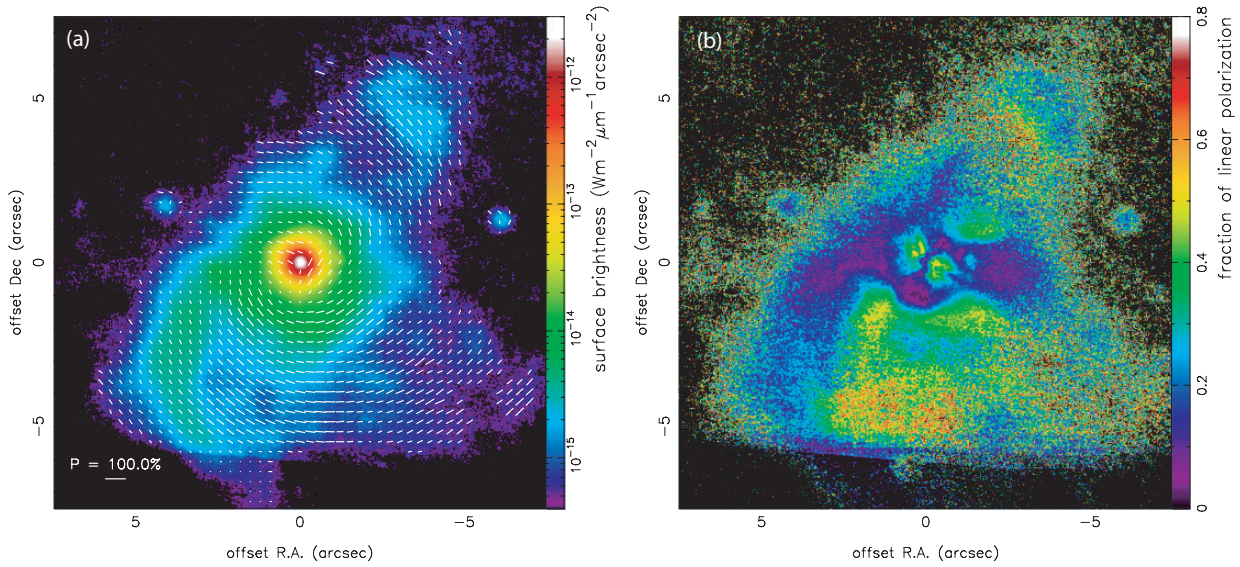

Fig. 1. Results of H-band imaging polarimetry of IRAS 19312+1950. The field of view is 15″ × 15″. **a)** The total intensity (Stokes I) image. The polarization vectors are also plotted every 14 pixels (~0.″3). **b)** The fraction of linear polarization map. The poor image quality 2″ from the bottom is due to the lack of data in some dither positions.

to explain observed spectral energy distributions (SEDs) and images, as well as to investigate the stellar parameters, are important. Although dust is expected to contribute only ~1% of the mass in the envelope (e.g. Knapp & Kerr 1974), it plays a more important role in the transfer of radiation from the optical to far-infrared (FIR) than does gas. Furthermore, light scattered by dust in the envelope often dominates in the SED at optical and near-infrared (NIR) wavelengths, and the maximum dust grain size in envelopes around AGB stars and post-AGB stars is expected to be on the order of 0.1 μm (e.g. Jura 1996). Polarization analysis in the NIR is a powerful technique for probing such a dusty environment. In our experiments, therefore, we performed imaging polarimetry of the IRAS 19312+1950 nebula in the NIR and radiative transfer modeling to derive the stellar parameters and dust properties in the envelope by comparing these with the observed SEDs, the total intensity image, and the polarization properties. The results of our observations and numerical simulations are presented in Sects. 2 and 3, respectively. In Sect. 4, we discuss the properties of dust in the envelope and the central star of IRAS 19312+1950.

2. Observations and results

2.1. H-band imaging polarimetry

We obtained polarimetric images of IRAS 19312+1950 using the NIR camera (CIAO) on the 8 m Subaru telescope on 2 August 2002. Because the object is faint in the J-band (m_J = 11.3 mag) and the nebulosities are easier to detect in the H band than the K-band, we only tried the H-band in this experiment. The central wavelength and the band width of the H-band filter are λ_c = 1.65 μm and $\Delta\lambda$ = 0.30 μm, respectively. We used the medium-resolution camera with a 0.0217 arcsec pix^{-1} pixel scale (22″ × 22″ field of view (FOV)). Since the target is too faint at the wavelength for adaptive-optics (AO) wavefront sensing (m_R = 18 mag), the AO was not used. The natural seeing was ~0.″6 at H-band, and we followed the observing sequence described in our previous paper (Murakawa et al. 2005). To measure linear polarization, we obtained four sets of images with orientations of the half-wave plate (HWP) of 0°, 45°, 22.5°, and 67.5°. The exposure time for each frame acquisition was 3 s. Five frames were obtained for each orientation of the HWP and eight dither offsets of 10″ separation were performed. The total integration time was 480 s. The nebula of the target covers the entire FOV of the camera, and complex interstellar diffuse emission and polarization are expected (Axson & Ellis 1976) because the target is located near the galactic plane (galactic coordinate of 55.°37, +0.°185). Thus, we also obtained sky frames for calibration of the sky background level and interstellar polarization. The position offsets are 20″ east and west of the target. The same observing procedures as those of the target were applied.

We reduced the observed data in a similar manner as described in our previous papers (Murakawa et al. 2004, 2005). We first subtracted the dark frame and applied flat-fielding. We calibrated the sky background level and the interstellar polarization by subtracting the sky frames. Then we obtained the Stokes IQU images, converting with formula $I = (I_{0.0} + I_{22.5} + I_{45.0} + I_{67.5})/2$, $Q = (I_{0.0} - I_{45.0})/\eta$, and $U = (I_{22.5} - I_{67.5})/\eta$. Where η is the total polarization efficiency of the HWP and the wire-grid polarizer, the value of 0.875 (Murakawa et al. 2004) was used in this experiment. The polarized intensity (PI), the fraction of linear polarization (P), and the polarization position angle (θ) were also derived by $PI = \sqrt{Q^2 + U^2}$, $P = PI/I$, and $\theta = 1/2 \arctan(U/Q)$, respectively. We also obtained error images of all Stokes parameters, the fraction of linear polarization, and the polarization position angle. The signal-to-noise ratios of the Stokes I image are 7–10 in a region within 1″ from the central star and 30–60 in a region ~3″ from the central star. The estimated background surface brightness and the polarization in the neighboring sky are 7×10^{-15} W m^{-2} μm^{-1} arcsec^{-2} (13.0 mag arcsec^{-2}, cf. 13.4 mag arcsec^{-2} for the averaged sky background level, Tokunaga 2000) and 1–2%, respectively. The error of linear polarization is 2–5% per pixel.

2.2. Polarization map

Figures 1a and b present a total intensity map (Stokes I) with polarization vectors and a fraction of linear polarization map, respectively. The field of view (FOV) is 15″ × 15″. Figure 2

shows what is seen in our images. The total intensity map shows a nearly spherical nebulosity within 3″ of the intensity peak, two ring-like structures extending ∼10″ to the northwest and the southeast (PA of −37° with respect to the intensity peak), and a lobe extending southwest. The ring-like structures look rather point-symmetric. These nebulous features are seen as a horn-like structure in the 2MASS *JHK*-band images (Nakashima & Deguchi 2000) and an NIR image (Deguchi et al. 2004). The polarization vectors are centro-symmetrically aligned in the entire nebula, where a sufficient signal is detected, and the fraction of linear polarization attains 30–60% in nebulosities at NW, SE, and SW. These features suggest that the nebulosity is seen with singly-scattered light in the *H*-band, which is emitted from the central star, and the nebulae are associated with the central star. In the fraction of linear polarization map, we see low polarization ($P < 20\%$) in the SE and NW arms. A possible interpretation is scattering angle dependence of polarization properties. The fraction of linear polarization has its maximum value near the normal scattering angle and lower values in forwardly or backwardly scattered light (see Fig. 2 in the paper by Fischer et al. 1994). If we assume that the S-shaped arm has a physically ring-like dust structure and the plane of the ring is tilted with respect to the plane of the sky, the scattered light from the ring is expected to have low polarizations. Such a polarization distribution is remarkably different from IRAS 17441–2441 (Oppenheimer et al. 2005), in which polarization is enhanced at the rim of the bipolar lobes. In this object, the bipolar lobes are hollow and light scattered at the rim in the plane of the sky results in a large fraction of polarization. The different characteristics in the polarization map of IRAS 19312+1950 are due to a different density structure of its nebula. We also identifie two spots with high polarization within 1″ of the central star. The spots are aligned in the equatorial direction; i.e., perpendicular to the polar direction. A similar signature is seen in an optically thin nebula with an equatorially enhanced density distribution (e.g. Murakawa et al. in prep.). It may be possible that dust condenses more in the equatorial direction than in the polar axis. However, it is slightly suspicious because of the natural seeing-limited angular resolution (∼0.″6 at *H*-band) in our image.

We compare our NIR image with the results of previous CO observations (Nakashima & Deguchi 2005). Narrow components of 35–36 and 37–38 km s^{-1} in ^{13}CO $J = 1$–0 emission lines extending ∼20″ roughly correspond to the NW and SE arms. Because the velocity distribution does not suggest any rotating motion, the narrow components could represent a bipolar outflow rather than a disk or a spherically expanding shell. The NW and SE arms are blue- and red-shifted components, respectively, while the NW arm is fainter than the SE one. This cannot be explained with the inclination effect of the nebula. Broad components in ^{12}CO and ^{13}CO only appear around the central star with ∼5″ radii. It could reflect the inner core, as seen in our NIR image. We will discuss more details of these narrow and broad components in Sect. 4.2.

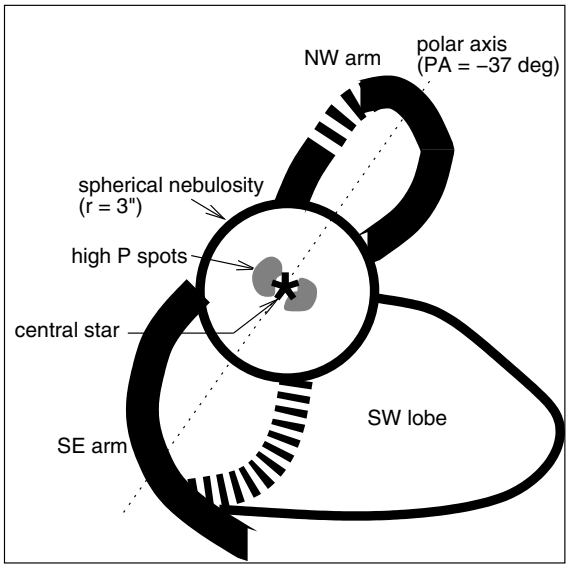

Fig. 2. This cartoon explains what is detected in our images.

3. Radiative transfer modeling

3.1. Model assumptions

We performed radiative transfer calculations to estimate the stellar parameters and to investigate the dust properties in the envelope. We used a Monte Carlo code, which simulates thermal emission and light scattering by dust grains in a model geometry (Ohnaka et al. 2006). This code computes the SEDs and a dust temperature distribution and generates Stokes *IQUV* images. Our code was applied to interpret the mid-infrared spectro-interferometric data of the silicate carbon star IRAS 08002–3803 (Ohnaka et al. 2006) and the near-infrared polarimetric data of the bipolar proto-planetary nebula (PPN) Frosty Leo (Murakawa et al. in prep.).

Although attempts to estimate the stellar parameters have been made, they are still uncertain. Nakashima et al. (2004) estimated a distance ranging between 2.5 and 3.9 kpc by applying the bolometric luminosity of 8000 $L_\odot$, which is typical of AGB stars. The lower limit is obtained if the estimated interstellar extinction of $A_V = 16.3$ mag from their CO-integrated intensity ($V_{\rm lsr} = 27$–33 km s^{-1} component) is assumed to be from a foreground cloud. If it is from a background cloud, the upper limit is obtained. Following Nakashima et al. (2004), we apply the distance d of 2.5 kpc in our modeling and discuss the effect of the distance on the luminosity in Sect. 4.1 The stellar effective temperature is also not well known, but is expected to be less than 4000 K, taking the possible spectral type of a late K or an M giant into account (Wood, P. R. 2002, private communication). The bolometric luminosity and the stellar temperature are estimated by SED fitting.

The detection of several oxygen-rich molecular lines (e.g. masers of SiO and H_2O, Nakashima & Deguchi 2000) and a weak absorption feature at 10 μm (Volk et al. 1991) indicate an oxygen-rich environment in the envelope. Therefore, we assume bare silicate grains. We use the optical constants of astronomical silicate (Draine 1985). To simplify the grain model, we apply a spherical shape with an MRN-like power law size distribution; i.e., $a_{\rm min} \le a \le a_{\rm max}$ and $n(a) = a^{-3.5}$, where a and $n(a)$ are the grain radius and the size distribution function, respectively (Mathis et al. 1977). In our Monte Carlo experiments, the size-distribution averaged values of the opacities and the scattering matrix components are used, which are given by

$$\langle X \rangle = \int_{a_{\rm min}}^{a_{\rm max}} X(a)\, n(a)\, {\rm d}a \Big/ \int_{a_{\rm min}}^{a_{\rm max}} n(a)\, {\rm d}a,$$

where X is the extinction cross section $C_{\rm ext}$, the absorption cross section $C_{\rm abs}$, or the scattering amplitude matrix elements $S_1(\theta)$ or $S_2(\theta)$. The averaged scattering cross section $C_{\rm sca}$ is given by $\langle C_{\rm sca} \rangle = \langle C_{\rm ext} \rangle - \langle C_{\rm abs} \rangle$. We set the minimum grain size $a_{\rm min}$ to

Table 1. Model parameters.

parameters	adopted values	comments
	stellar model	
$T_{\rm eff}$	2800 K	by SED fit
$L_\star$	7000 $L_\odot$	by SED fit
d	2.5 kpc	adopted
$R_\star$	2.5×10^{13} cm	calculated
$\alpha_\star$	0.66 mas	calculated
	model geometry	
$R_{\rm in}$	7 $R_\star$	by SED fit
$R_{\rm tr}$	50 $R_\star$	by SED fit
$R_{\rm out}$	23 000 $R_\star$	adopted
τ	20 (V), 1.5 (H)	by SED fit
β_1	2	adopted
β_2	0.8	by SED fit
	grain model	
$a_{\rm min}$	0.005 μm	adopted
$a_{\rm max}$	0.3 μm	by polarization fit
$n(a)$	$a^{-3.5}$	adopted

be 0.005 μm, since there is no other crucial clue for determining it. The maximum grain size $a_{\rm max}$ is constrained by our modeling.

The IRAS 19312+1950 nebula already shows a distinct and complex bipolar appearance in the ∼10″ scale FOV. However, in our modeling, we focus on estimating fundamental properties such as the stellar temperature, the bolometric luminosity, the dust envelope mass, and the present-day mass-loss rate instead of reproducing the ring-like structure. Because the inner core ($r < 3''$) has a nearly spherical structure, although an indication of asymmetry is expected, we apply one-dimensional spherically symmetric geometries, and such an approximation would satisfy our science goal. The outer radius $R_{\rm out}$ is set to be a fixed value of 23 000 $R_\star$, which corresponds to the extension of the nebula of ∼15″ detected in the 2MASS *JHK*-band images, assuming the distance of 2.5 kpc. Since two origins of dust (i.e., the stellar system and ambient clouds) have been suspected before, we assume a model geometry with a radial density profile given by $\rho\,(r) = \rho_1\,(r/R_{\rm in})^{-\beta_1} + \rho_2\,(r/R_{\rm in})^{-\beta_2}$, where $R_{\rm in}$ is the inner radius of the dust shell and the densities of two components become equal at a transition radius $R_{\rm tr}$. The values of ρ_1 and ρ_2 are determined from an input value of the radial optical depth of the shell (τ).

3.2. Model results

We found that exponent values of $\beta_1 = 2$ and $\beta_2 = 0.8$ produce the best-fit of the mid-infrared SED, in particular the self-absorption silicate feature around 10 μm. With respect to the grain properties, we obtained the maximum grain size of $a_{\rm max} = 0.3\ (\pm 0.05)$ μm, which satisfies the fraction of linear polarization of our observational result. The extinction cross section $C_{\rm ext}$, the dust albedo ω, and the scattering asymmetry g-parameter at 1.65 μm are 8.47×10^{-7} cm^2, 0.389, and 0.187, respectively. We searched the following parameter ranges: $T_{\rm eff}$ of 2500 to 3000 K with a 100 K step, $L_\star$ of 5000 to 10 000 $L_\odot$ with a 1000 $L_\odot$ step, $R_{\rm in}$ of 3, 5, 7, and 10 $R_\star$, $R_{\rm tr}$ of 10, 30, 50, and 100 $R_\star$, and τ_V of 7, 10, 20, and 50. These combinations yield 2304 models, and we have examined their SEDs. The best fit model has $T_{\rm eff} = 2800\ (\pm 100)$ K, $L_\star = 7000\ (\pm 1000)$ $L_\odot$, $\tau_V = 20$ (1.5 at 1.65 μm), $R_{\rm in} = 7$ $R_\star$, and $R_{\rm tr} = 50$ $R_\star$. The stellar radius $R_\star$ and its apparent size at 2.5 kpc are 2.5×10^{13} cm and 0.66 mas, respectively. The model parameters are summarized in Table 1.

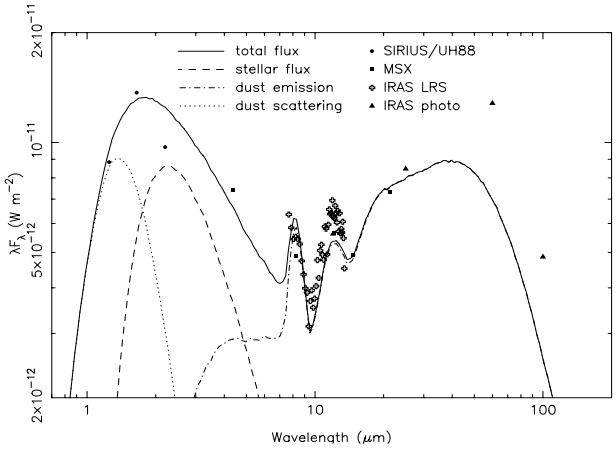

Fig. 3. A comparison of the model SED with the observational results. The solid, dotted, dashed, and dashed-dotted curves denote the model results of the total flux, scattered light by dust in the envelope, the attenuated stellar flux, and the thermal emission from the envelope, respectively. The filled circles, filled squares, open crosses, and filled triangles are from the photometric results using SIRIUS on the UH88 telescope and MSX, the IRAS low-resolution spectrum (LRS), and the IRAS photometry, respectively. The estimated interstellar extinction of $A_V = 16.3$ mag is corrected in the SIRIUS data. The estimated background contributions of 30% and 62% of the 60 and 100 μm flux are subtracted from the IRAS photometry.

The SED of the best model was compared with the observed SEDs in Fig. 3. The data are from from *JHK*-band photometry obtained using the SIRIUS camera on the University of Hawai'i 88-inch telescope (UH88), which is dereddened with $A_V = 16.3$ mag to correct for the foreground extinction (Nakashima et al. 2004), the Mid-course Space eXplorer (MSX) point source catalogue, the InfraRed Astronomical Satellite (IRAS) low-resolution spectrum (LRS), and the IRAS photometry. Because IRAS 19312+1950 is located near the Galactic plane, a large fraction of flux in FIR is expected from background emission (Izumiura et al. 1999). We obtain a rough estimation of the background contributions of 30% at 60 μm and 62% at 100 μm from the IRAS Sky Survey Atlas (ISSA). Since the pixel scale of the images is 1.″5, the target is unresolved and seems to be located in a region with complex emission features; the true values could exceed the above values. These background contributions are subtracted from the results of 60 and 100 μm IRAS photometry, plotted in Fig. 3. Scattered light from the dust shell and the stellar flux dominates at wavelengths shorter than 5 μm, while the thermal emission from the dust shell does at longer wavelengths. The dust temperatures at the transition radius (50 $R_\star$) and at the inner boundary of the shell (7 $R_\star$) are 290 K and 960 K, respectively. The inner boundary temperature suggests a steady formation of fresh dust in the outflow as oxygen-rich dust starts to condense at temperatures typically in the range 1000–1500 K. The flux from the inner shell mainly contributes at wavelengths shorter than 10 μm and the flux from the outer shell at longer wavelengths. Our model SED is in fair agreement with the IRAS LRS 10 μm spectrum, which shows the silicate self-absorption (Volk et al. 1991). The FIR flux of our model results are sufficiently lower than the background subtracted results of the IRAS photometry at 60 and 100 μm. The possible reasons are that our model geometry (i.e., one-dimensional spherical model) is too simple and the estimation of background contribution is too low, as already described.

The applied distance of 2.5 kpc in the above analysis is based on an assumption that all CO emissions of $V_{\rm lsr}$ = 27–33 km s^{-1} component are from foreground clouds (Nakashima et al. 2004). It is hard to determine the distance to the object in general. However, it may be possible to be constrained by taking the contribution of the interstellar extinction into account. If all CO emissions are assumed to be from background, the distance to the object is estimated to be 3.9 kpc (Nakashima et al. 2004). This results in all foreground extinctions being due to the interstellar extinction of A_V = 6.2 mag applying the standard interstellar extinction (e.g. Allen 1973; Deguchi et al. 1998) and the optical depth of the envelope of τ_V = 31. We perform some modeling with different contributions from the foreground extinction between 6.2 and 16.3 mag. We find that a model with $\tau_V > 23$ (i.e., a foreground extinction $A_V < 14.9$ mag) fits the observed SED, and a high A_V is preferred to a low A_V. Thus, it is likely that the object is near the rear side edge or behind ambient clouds. Then we take the contribution of the interstellar extinction into account with a fixed foreground cloud component. We find good solutions in the SED fit when the interstellar extinction A_V is between 2.2 and 6.7 mag. From this result, we estimate a possible distance to be between 1.4 and 4.2 kpc.

We also made Stokes *IQU* images with another Monte Carlo experiment. Since the thermal emission is negligible in the *H*-band, as seen in the SED (Fig. 3), we used monochromatic light at a wavelength of 1.65 μm to obtain Stokes images at a particular wavelength much more efficiently than the full radiation transfer mode, which is applied when calculating SEDs. In this fixed wavelength mode, a photon packet is always scattered at an interacting point, and the weight of the photon packet is reduced by a factor equal to the dust albedo ω. The output Stokes images were convolved with a Gaussian function with a 0.″6 diameter, which corresponds to the observed PSF size in the *H*-band. Figure 4a shows a comparison of a radial intensity (Stokes *I*) distribution of our model to the azimuthally averaged observational result. Our observational result can be actually fit with β = 1.2 if a single power law is applied. However, it provides a poorer fit of the 10 μm silicate self-absorption feature and too low a flux in the FIR, and we could not find any adequate solutions to fit the observed SED and the radial intensity distribution simultaneously with a single power-law model. Although we see somewhat steep and shallower slopes in our two-component model within 0.″9 from the central star and further, respectively, the two-component model can reproduce the observed data reasonably well. Figure 4b shows the radial profile of the fraction of linear polarization. Since there are regions with small polarizations along the S-shaped arm, we omitted the data towards the central star within $r < 1.''3$ because of contamination by unpolarized light from the central star PSF. On the other hand, the linear polarization increases gently for $r > 1.''3$. Although our observational result of the radial profile has a somewhat complex shape because of the S-shaped arm in the bipolar nebula, the overall shape of our model result agrees well with our observational data. Changing the maximum grain size does not affect the shape of the radial profile much, but it does change the absolute fraction of linear polarization dramatically. For a smaller $a_{\rm max} < 0.25$ μm, a higher polarization >45% is attained, and for a larger $a_{\rm max} > 0.37$ μm, a lower polarization <35% at $r = 4.''5$ is attained.

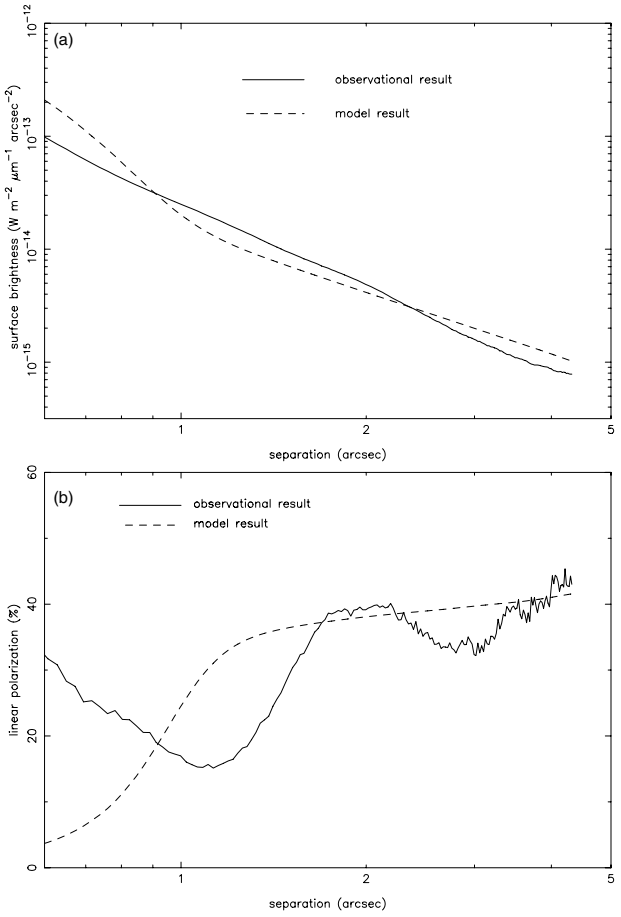

Fig. 4. The radial profiles of the total intensity **a)** and linear polarization **b)**, respectively. The solid curve and the dashed curve denote the observational result and the model result, respectively.

4. Discussion

The puzzling thing about IRAS 19312+1950 is that this object shows characteristics of several object classes. The reported massive envelope (Deguchi et al. 2004) and an extremely high mass-loss rate are reminiscent of a supergiant. However, some C- and N-bearing molecules in the envelope, such as NH_3, SO, H_2CS, and CH_3OH (Deguchi et al. 2004) are the ones often detected in dark clouds. The detection of SiO (and H_2O) masers and a stronger OH maser satellite line at 1612 MHz than main lines at 1665 and 1667 MHz suggest an AGB star or a post-AGB star. Furthermore, an FIR emission distribution ($\geq 1'$) extends sufficiently more than the nebulosity seen in the NIR (~30″). As already suspected, these characteristics are probably caused by contributions from the matter originated outside the object; i.e., ambient clouds (Deguchi et al. 2004; Nakashima & Deguchi 2005). Thus, we discuss the properties of the central star and the dust in the envelope separately.

4.1. Stellar properties

From our radiative transfer modeling, the stellar temperature and the distance are estimated to be $T_{\rm eff}$ = 2800 K and d = 1.4–4.2 kpc, respectively. The uncertainty of the distance causes the estimated luminosity ($1100d^2$ $L_\odot$) to range between 2200 $L_\odot$ and 19 000 $L_\odot$. With these properties, the object class of IRAS 19312+1950 could be classified in the Hertzsprung-Russell diagram. Considering YSOs, low-mass YSOs are much fainter ($L_\star < 10$ $L_\odot$, e.g. Hartigan et al. 1995; Whitney et al. 2004), and luminous YSOs such as Herbig Ae/Be stars are much hotter ($T_{\rm eff} > 4000$ K) (see also Fig. 1 of theoretical

pre-main sequence tracks in the HR diagram presented by Palla & Stahler 1999). Thus, IRAS 19312+1950 is unlikely to be a YSO. Considering evolved stars, it is also unlikely to be a supergiant because the estimated luminosity of IRAS 19312+1950 is within the AGB limit ($\sim 5 \times 10^4\ L_\odot$, Paczyński 1971; Wood et al. 1983) and is sufficiently lower than several known supergiants; e.g. $7 \times 10^5\ L_\odot$ for IRC +10 420 (Jones et al. 1993), $2 \times 10^5\ L_\odot$ for NML Cyg (Blöcker 2001), $5.5 \times 10^5\ L_\odot$ for VY CMa (Sopka et al. 1985). Therefore, the possibility remains that IRAS 19312+1950 is an AGB or a post-AGB star.

From our modeling, we estimate the dust-envelope mass to be 0.14 $M_\odot$ if the distance to the object of 2.5 kpc is applied. Comparing this with a gas envelope mass of ~25 $M_\odot$ (Deguchi et al. 2004), the gas-to-dust mass ratio is found to be ~180:1, which is very typical for the neutral interstellar medium in the galactic plane and the winds of AGB stars of about solar metallicity (Knapp & Kerr 1974; Knapp 1985). We also estimate a mass-loss rate. While the value of $2.6 \times 10^{-4}\ M_\odot\ \mathrm{yr}^{-1}$ obtained by Deguchi et al. (2004) is derived at $r \sim 3''$ from the central star, our modeling allows us to derive the current value. Applying the above gas-to-dust mass ratio and the expansion velocity of 25 $\mathrm{km\,s^{-1}}$, which is approximately half the width of the CO J = 1–0 emission velocity distribution (Nakashima et al. 2004), we obtain the current mass-loss rate of $5.3 \times 10^{-6}\ M_\odot\ \mathrm{yr}^{-1}$. This value is in good agreement with the value of $6.3 \times 10^{-6}\ M_\odot\ \mathrm{yr}^{-1}$ calculated with an empirical formula of mass-loss rate $\log \dot{M} = -5.65 + 1.05 \log (L/10\,000\ L_\odot) - 6.3 \log (T_{\mathrm{eff}}/3500\ \mathrm{K})$ for M-type AGB stars (van Loon et al. 2005). From the above properties, the central star of IRAS 19312+1950 shows characteristics of dust-enshrouded AGB stars.

4.2. Nebula and duality of the dust chemistry

Dust shells formed in the AGB phase often have a nearly spherical shape, as seen in TT Cyg (Olofsson et al. 2000) and in large field of view (>10″) images of IRC +10 216 (Mauron & Huggins 2000). Bipolarity, which is seen in a large fraction of PNs (Corradi & Schwarz 1995), is thought to be formed by the fast wind during the PPN phases (e.g. review by Balick & Frank 2002). However, the evidence of high-velocity jets and a rotating disk have been reported in some AGB stars, which are not thought to undergo the intensive mass loss that forms an aspherical dust shell; e.g., V Hya (Kahane et al. 1996; Sahai et al. 2003; Hirano et al. 2004), X Her (Kahane & Jura 1996; Nakashima 2005), and RV Boo (Bergman et al. 2000). These facts are hard to explain with a scenario of the stellar evolution of a single star, and it is thought that binary companion(s) must play an important role in shaping aspherical shells (e.g. Soker 1997, 2002). With respect to IRAS 19312+1950, the S-shaped arm is detected in NIR images, and such a morphology might be the result of interactions with binary companions. However, while the high-velocity, broad components are extended and seen as a bipolar outflow, and narrow components concentrate close to the central star in the case of V Hya, the kinematic properties in IRAS 19312+1950 are opposite. A possible interpretation is given as follows: the object is probably embedded in an ambient cloud. The fast wind from the central star, which is detected in the broad components in ^{12}CO and ^{13}CO, rapidly slows down due to the thick ambient cloud matter. As a result, the narrow components of 35–36 and 37–38 $\mathrm{km\,s^{-1}}$ in ^{13}CO J = 1–0 extending ~15″ towards the NW and SE directions are seen.

The duality of dust chemistry, i.e., detection of C- and O-bearing molecules, in the IRAS 19312+1950 nebula is also an interesting issue. Carbon stars with oxygen-rich molecules in the envelope, such as silicate carbon stars (Little-Marenin 1986; Willems & de Jong 1986) and the Red Rectangle (Waters et al. 1998), are known or are expected to have binary companions. The most widely accepted hypothesis for the presence of oxygen-rich dust in envelopes around these carbon stars suggests that silicate was ejected by mass loss from the primary star and was trapped in a circumbinary disk or a companion disk when the primary carbon star was an M giant (Morris 1987; Lloyd-Evans 1990). Evidence of a disk or a reservoir is obtained when a narrow velocity component ($v < 5\ \mathrm{km\,s^{-1}}$) is detected in CO emission lines (e.g. Kahane et al. 1998). With respect to IRAS 19312+1950, the detection of SiO maser emissions (Nakashima & Deguchi 2000) presents a strong constraint on the nature of the central star. The SiO maser emissions have been detected toward evolved stars with only a few exceptional star-forming regions; e.g., Orion-KL (Baud et al. 1980) and W51 IRS2 (Fuente et al. 1989) and are produced above the surface (5–10 AU or a few $R_\star$) of evolved stars (Elitzur 1980). To date, no detection has been reported in a silicate carbon star (e.g. Nakada et al. 1987) or in any other carbon star (e.g. Lepine et al. 1978; Schöier et al. 2006). Thus, IRAS 19312+1950 is probably an oxygen-rich star, at least at this moment, and C-bearing molecules do not originate in the mass loss from the central star. The origin of C- and N-bearing molecules, which are detected towards IRAS 19312+1950, could be chemical reactions in the wind (Lindqvist et al. 1988; Willacy & Millar 1997; Duari et al. 1999) or ambient cloud matter, which kinetically merges with the matter ejected by the mass loss from the central star.

5. Conclusion

We present H-band imaging polarimetry of the peculiar bipolar nebula IRAS 19312+1950 using CIAO on the Subaru telescope. The total intensity image clearly shows a point-symmetric S-shaped arm extending towards the northwest and the southeast. The polarization map revealed a centro-symmetric polarization vector pattern in the entire bipolar lobes with polarizations of 30–60%. These results indicate that the nebulae are associated with the central star and are seen in light scattered by dust in the nebula. We find low polarizations ($P < 20\%$) on the east side of the SE and NW arms, suggesting that the S-shaped arm has a physically ring-like structure instead of a hollow or cavity structure in the lobes.

We also investigated the physical properties of the central star and the nebula by means of radiative transfer calculations for dust. The estimated stellar temperature and bolometric luminosity are 2800 K and 7000 $L_\odot$, respectively. The distance uncertainty is found to be between 1.4 and 4.2 kpc. Comparing the gas envelope mass of 25 $M_\odot$ to the dust envelope mass of 0.14 $M_\odot$, the gas-to-dust mass ratio obtained is 180:1. With this value, the current mass-loss rate is estimated to be $5.3 \times 10^{-6}\ M_\odot\ \mathrm{yr}^{-1}$. This is in good agreement with the value of $6.3 \times 10^{-6}\ M_\odot\ \mathrm{yr}^{-1}$ calculated with an empirical mass-loss formula for M-type AGB stars. From the above stellar properties and detections of SiO, H_2O, and OH masers, the central star of IRAS 19312+1950 shows characteristics of an oxygen-rich, dust-enshrouded AGB star rather than a YSO or a supergiant.

Our results support the idea (Deguchi et al. 2004; Nakashima & Deguchi 2005) that the object is embedded in ambient clouds, because the large envelope mass of 25 $M_\odot$ is impossible to explain with only mass loss from the possible AGB central star. Although the detected C- and N-bearing molecules can form by chemical reactions in the oxygen-rich envelope, it could also

originate from ambient cloud matter, which kinetically merges with the outflow of the central star.

Acknowledgements. We would like to thank the referee, Dr. J. Th. van Loon, for his particularly thoughtful comments that led to a significant improvement in this paper. We would also like to thank Drs. B. M. Lewis and P. R. Wood for providing us with the observational results of OH masers and *K*-band spectra of IRAS 19312+1950, respectively.

References

Allen, C. W. 1973, Astrophysical Quantities, 3rd ed. (London: Athlone Press)
Axson, D. J., & Ellis, R. S. 1976, MNRAS, 177, 499
Balick, B., & Frank, A. 2002, ARA&A, 40, 439
Baud, B., Bieging, J. H., Plambeck, R., et al. 1980, in Interstellar Molecules, ed. B. H. Andrew (Dordrecht: Reidel), 545
Bergman, P., Kerschbaum, F., & Olofsson, H. 2000, A&A, 353, 257
Blöcker, T., Balega, Y., Hofmann, K.-H., & Weigelt, G. 2001, A&A, 369, 142
Corradi, R. L. M., & Schwarz, H. E. 1995, A&A, 293, 871
Deguchi, S., Matsumoto, S., & Wood, P. R. 1997, PASJ, 50, 597
Deguchi, S., Nakashima, J., & Takano, S. 2004, PASJ, 56, 1083
Draine, B. T. 1985, ApJS, 57, 587
Duari, D., Cherchnesff, I., & Willacy, K. 1999, A&A, 341, L47
Elitzur, M. 1980, ApJ, 240, 553
Fischer, O., Henning, Th., & Yorke, H. W. 1994, A&A, 284, 187
Fuente, A., Martín-Pintado, J., Alcolea, J., & Barcia, A. 1989, A&A, 223, 321
Hartigan, P., Edwards, S., & Ghandour, L. 1995, ApJ, 452, 746
Hirano, N., Shinnaga, H., Dinh-V-Trung, et al. 2004, ApJ, 616, L43
Izumiura, H., Deguchi, S., Fujii, T., et al. 1999, ApJS, 125, 257
Jones, T. J., Humphreys, R. M., Gehrz, R. D., et al. 1993, ApJ, 411, 323
Jura, M. 1996, ApJ, 472, 806
Kahane, C., & Jura, M. 1996, A&A, 310, 952
Kahane, C., Audinos, P., Barnbaum, C., & Morris, M. 1996, A&A, 314, 871
Kahane, C., Barnbaum, C., Uchida, K., Balm, S. P., & Jura, M. 1998, ApJ, 500, 466
Knapp, G. R. 1985, ApJ, 293, 273
Knapp, G. R., & Kerr, F. J. 1974, A&A, 35, 361
Lepine, J. R. D., Scalise, E., & Le Squeren, A. M. 1978, ApJ, 225, 869
Lindqvist, M., Nyman, L.-A., Olofsson, H., & Winnberg, A. 1988, A&A, 205, L15
Little-Marenin, I. R. 1986, ApJ, 307, L15
Lloyd-Evans, T. 1990, MNRAS, 243, 336
Mathis, J. S., Rumpl, W., & Nordsieck, K. H. 1977, ApJ, 217, 425
Mauron, N., & Huggins, P. J. 2000, A&A, 359, 707
Morris, M. 1987, PASP, 99, 1115
Murakawa, K., Suto, H., Tamura, M. et al. 2004, PASJ, 56, 509
Murakawa, K., Suto, H., Oya, S., et al. 2005, A&A, 436, 601
Murakawa, K., Ohnaka, K., Driebe, Th., et al. 2006, in prep.
Nakada, Y., Izumiura, H., Onaka, T., et al. 1987, ApJ, 323, L77
Nakashima, J. 2005, ApJ, 620, 943
Nakashima, J., & Deguchi, S. 2000, PASJ, 52, L43
Nakashima, J., & Deguchi, S. 2005, ApJ, 633, 282
Nakashima, J., Deguchi, S., & Kuno, N. 2004, PASJ, 56, 193
Ohnaka, K., Driebe, T., Hofmann, K.-H., et al. 2006, A&A, 445, 1015
Olofsson, H., Bergman, P., Lucas, R., et al. 2000, A&A, 353, 583
Oppenheimer, B. D., Bieging, J. H., Schmidt, G. D., et al. 2005, ApJ, 624, 957
Paczyński, B. 1971, Acta. Astr., 21, 417
Palla, F., & Stahler, S. W. 1999, ApJ, 525, 772
Sahai, R., Morris, M., Knapp, G. R., Young, K., & Barnbaum, C. 2003, Nature, 426, 261
Schöier, F. L., Fong, D., Olofsson, H., Zahng, Q., & Patel, N. 2006, ApJ, 649, 965
Soker, N. 1997, ApJS, 112, 487
Soker, N. 2002, A&A, 386, 885
Sopka, R. J., Hildebrand, R., Jaffe, D. T., et al. 1985, ApJ, 294, 242
Tokunaga, A. T. 2000, in Chapter 7, in Allen's Astrophysical Quantities, 4th edition, ed. A. N. Cox (NY: Springer-Verlag), 143
van der Veen, W. E. C. J., & Habing, H. J. 1988, A&A, 194, 125
van Loon, J. Th., Cioni, M.-R. L., Zijlstra, A. A., & Loup, C. 2005, A&A, 438, 273
Volk, K., Kwok, S., Stencel, R. E., & Brugel, E. 1991, ApJS, 77, 607
Waters, L. B. F. M., Cami, J., de Jong, T., et al. 1998, Nature, 391, 868
Whitney, B. A., Indebetouw, R., Bjorkman, J. E., & Kenneth, W. 2004, ApJ, 617, 1177
Willacy, K., & Millar, T. J. 1997, A&A, 324, 237
Willems, F., & de Jong, T. 1986, ApJ, 309, L39
Wood, P. R., Bessel, M. S., & Fox, M. W. 1983, ApJ, 272, 99